

<sup>1</sup> **Estimating  $\chi$  and  $K_T$  from fast-reponse thermistors on traditional shipboard**

<sup>2</sup> **CTDs: sources of uncertainty and bias.**

<sup>3</sup> Andy Pickering\*

<sup>4</sup> *College of Earth, Ocean, and Atmospheric Sciences, Oregon State University, Corvallis, OR.*

<sup>5</sup> Jonathan Nash

<sup>6</sup> *College of Earth, Ocean, and Atmospheric Sciences, Oregon State University, Corvallis, OR.*

<sup>7</sup> Jim Moum

<sup>8</sup> *College of Earth, Ocean, and Atmospheric Sciences, Oregon State University, Corvallis, OR.*

<sup>9</sup> Jen MacKinnon

<sup>10</sup> *UCSD / Scripps Institute of Oceanography*

<sup>11</sup> \*Corresponding author address: College of Earth, Ocean, and Atmospheric Sciences, Oregon State University, Corvallis, OR.

<sup>13</sup> E-mail:

## ABSTRACT

14 The acquisition of turbulence data from traditional shipboard CTD casts is  
15 attractive, as its use could dramatically increase the amount of deep-ocean  
16 mixing observations globally. While data from shear-probes are easily con-  
17 taminated by motion of the instrument platform, the measurement of temper-  
18 ature gradient is relatively insensitive to vehicle vibration, making it possible  
19 to measure temperature gradient from a shipboard CTD rosette. The purpose  
20 of this note is to investigate the error and bias in estimating the rate of dissi-  
21 pation of temperature variance  $\chi$  and turbulent diffusivity  $K_T$  from traditional  
22 CTD casts. The most significant source of error is associated with the fact  
23 that fast-response FP07 thermistors resolve only a fraction of the tempera-  
24 ture gradient variance at the fallspeed of typical CTD casts. Assumptions  
25 must be made about the wavenumber extent of the temperature gradient spec-  
26 trum, which scales with the rate of dissipation of turbulent kinetic energy, a  
27 quantity that is not directly measured. Here we utilize observations from a  
28 microstructure profiler to demonstrate the validity of the method of estimat-  
29 ing  $\chi$  from thermistor data, and to assess uncertainty and bias. We then ap-  
30 ply this methodology to temperature gradient profiles obtained from  $\chi$ pods  
31 mounted on a CTD (the CTD- $\chi$ -pod), and compare these to microstructure  
32 profiles obtained almost synoptically at the equator. CTD- $\chi$ -pod estimates of  
33  $\chi$  compare favorably to the direct microstructure measurements and demon-  
34 strate that the  $\chi$ -pod method is not significantly biased. This supports the  
35 utility of the measurement as part of the global repeat hydrography program  
36 (GO-SHIP) cruises, during which this type of data has been acquired during  
37 the past few years.

<sup>38</sup> **1. Introduction**

<sup>39</sup> Turbulent mixing affects the distribution of heat, salt, and nutrients throughout the global ocean.

<sup>40</sup> Diapycnal mixing of cold, dense water with warmer water above maintains the abyssal overturning

<sup>41</sup> circulation (Munk 1966; Munk and Wunsch 1998), which affects global climate. Because the

<sup>42</sup> turbulence that drives mixing generally occurs at scales that are not resolved in climate models,

<sup>43</sup> it must be parameterized, based on either (i) aspects of the resolved model dynamics, (ii) through

<sup>44</sup> higher resolution models that capture the dynamics that feed energy to turbulence, or (iii) using

<sup>45</sup> other parameterizations that either dynamically or statistically quantify turbulent fluxes. Recent

<sup>46</sup> investigations have demonstrated that these models are sensitive to the magnitude and distribution

<sup>47</sup> of mixing (Melet et al. 2013). A comprehensive set of measurements that spans relevant dynamical

<sup>48</sup> regimes is needed to constrain mixing and develop more accurate parameterizations.

<sup>49</sup> Direct measurement of mixing with microstructure profilers equipped with shear probes is ex-

<sup>50</sup> pensive, time-intensive, and requires considerable care and expertise. Moreover, tethered profilers

<sup>51</sup> can't reach abyssal depths, requiring autonomous instruments to get deeper than  $\sim$ 1000-2000 m.

<sup>52</sup> As a result, existing measurements of diapycnal mixing, especially in the deep ocean, are sparse

<sup>53</sup> (Waterhouse et al. 2014). In order to obtain a larger quantity of mixing estimates, considerable

<sup>54</sup> work has gone into inferring mixing from measurements of the outer scales of turbulence, which

<sup>55</sup> are easier to obtain. One popular method is the use of Thorpe scales, where diapycnal mixing is

<sup>56</sup> inferred from inversions in profiles of temperature or density (Thorpe 1977; Dillon 1982). The

<sup>57</sup> size of resolvable overturn is limited by the profiling speed and instrument noise (Galbraith and

<sup>58</sup> Kelley 1996). Several studies indicate relatively good agreement with microstructure and other

<sup>59</sup> observations, but there are some questions about the validity of the method and the assumptions

<sup>60</sup> made (Mater et al. 2015; Scotti 2015). Parameterizations based on profiles of shear and/or strain

have also been developed and applied to estimate diapycnal mixing (Gregg 1989; Kunze et al. 2006; Polzin et al. 2013; Whalen et al. 2012, 2015). However, they rely on a series of assumptions about the cascade of energy from large to small scales that are often violated; numerous studies (i.e., Waterman et al. (2013)) have shown that there is significant uncertainty associated with these parameterizations, in that there can be a consistent bias in a particular region, yet the sense of the bias (i.e., overpredict vs. underpredict) is not known a priori.

Quanitifying turbulence from velocity shear variance (to compute the dissipation rate of turbulent kinetic energy  $\varepsilon$ ) is challenging on moorings or profiling platforms because there is usually too much vibration and/or package motion for shear-probes to be useful. Other methods (i.e., optics or acoustics) may hold some promise, but lack of scatterers often precludes this type of measurement, especially in the abyss. In addition, shear probes only provide  $\varepsilon$ , not the mixing of scalars,  $K$ , which is often inferred from  $\varepsilon$  by assuming a mixing efficiency  $\Gamma$  (Osborn 1980) as  $K = \Gamma \varepsilon / N^2$ , which  $N^2$  is the buoyancy frequency. A more direct measure of turbulent mixing is obtained from the dissipation rate of temperature variance  $\chi$  (Osborn and Cox 1972). This has the advantage that (i) the temperature and temperature gradient can be computed and is relatively straightforawrd to measure, and (ii) the estimation of mixing from  $\chi$  does not require assumptions about  $\Gamma$ . However, the spectrum of temperature gradient extends to very small scales, so that its spectrum is seldom fully resolved (and unlike shear variance, the wavenumber extent of the temperature gradient spectrum does not scale with its amplitude, but instead depends on  $\varepsilon$ ). Assumptions about the spectral shape (Kraichnan vs. Bachelor, and the value of the “constant”  $q$ ) and its wavenumber extent (governed by the Batchelor wavenumber  $k_b = [\varepsilon / (v D_T^2)]^{1/4}$  (Batchelor 1959)) are thus necessary to determine  $\chi$  unless measurements capture the full viscous-diffusive subrange of turbulence (i.e., down to scales  $\Delta x \sim 1/k_b \sim 1\text{mm}$ ), a criterion seldom achieved. To resolve this, we follow Al-

<sup>84</sup> ford and Pinkel (2000) and Moum and Nash (2009) and make the assumption that  $K_T = K_\rho$  to  
<sup>85</sup> determine the dissipation rate as  $\varepsilon_\chi = (N^2\chi)/(2\Gamma \langle dT/dz \rangle^2)$ , permitting  $k_b$  to be estimated.  
<sup>86</sup> The goal of this paper is to outline and validate the methods used to compute  $\chi$  and  $K_T$  with  
<sup>87</sup>  $\chi$ -pods mounted on CTDs. We do this by applying our processing methodology to profiles of tem-  
<sup>88</sup> perature gradient measured by thermistors on the ‘Chameleon’ microstructure profiler, which pro-  
<sup>89</sup> vides a direct test of our methodology. Because Chameleon is a loosely tethered profiler equipped  
<sup>90</sup> with shear probes (Moum et al 1995), it directly measures  $\varepsilon$  and allows us to test our assumptions.  
<sup>91</sup> Specifically, it allows us to determine biases associated with computing  $\chi$  from partially-resolved  
<sup>92</sup> temperature alone, as compared to that when it is computed by including knowledge of the dissi-  
<sup>93</sup> pation rate, which constrains the wavenumber extent of the scalar spectra. After establishing that  
<sup>94</sup> the method works, we then compare CTD- $\chi$ pod profiles to nearby microstructure profiles.

## <sup>95</sup> 2. Data

### <sup>96</sup> a. EQ14

<sup>97</sup> Data were collected on the R/V Oceanus in Fall 2014 during the EQ14 experiment to study  
<sup>98</sup> equatorial mixing. More than 2700 Chameleon profiles were made, along with 35 CTD- $\chi$ pod  
<sup>99</sup> profiles bracketed by Chameleon profiles in order to maintain calibrations during the cruise. Most  
<sup>100</sup> Chameleon profiles were made to a maximum depth of about 250m, with CTD casts going to  
<sup>101</sup> 500m or deeper. The EQ14 experiment and results are discussed in more detail in (SJ Warner, RN  
<sup>102</sup> Holmes, EH McHugh-Hawkins, JN Moum, 2016: Buoyant gravity currents released from tropical  
<sup>103</sup> instability waves, JPO, in preparation).

<sup>104</sup> **3. Methods**

<sup>105</sup> As mentioned in the introduction, the temperature gradient spectrum is rarely fully resolved  
<sup>106</sup> down to the small scales of turbulent mixing. The fraction of the spectrum resolved depends on  
<sup>107</sup> the true spectrum (a function of  $\chi$  and  $\varepsilon$ ), the flowspeed past the sensor ( $u$ ), and the response of  
<sup>108</sup> the thermistor. The GE/Thermometrics FP07 thermistors we use typically resolve frequencies up  
<sup>109</sup> to about 10-15 Hz. The maximum resolved wavenumber is then equal to  $k_{max} = f_{max}/u$ , while  
<sup>110</sup> the wavenumber extent of the true spectrum varies with  $k_b$  (and  $\varepsilon^{1/4}$ ). At the typical vertical  
<sup>111</sup> fall rate of a CTD rosette ( $\sim 1\text{m/s}$ ), only about 20% of  $k_b$  is resolved at  $\varepsilon = 10^{-10}\text{ W/kg}$  (Figure  
<sup>112</sup> 2). While methods have been developed to fit the observed temperature gradient spectrum to  
<sup>113</sup> theoretical forms (Ruddick et al. 2000), these work only when a larger fraction of the temperature  
<sup>114</sup> gradient spectrum is resolved. For the relatively high profiling speeds typical of CTD casts, we  
<sup>115</sup> find these methods do not work well (see appendix for details) and therefore we use the following  
<sup>116</sup> methodology, which does not have a strongly  $\varepsilon$ -dependant bias.

<sup>117</sup> We first outline our method for estimating  $\chi$ , which relies on (i) determining the instantaneous  
<sup>118</sup> flowspeed past the sensor, (ii) identifying periods where the signals may be contaminated by the  
<sup>119</sup> wake of the CTD rosette, (iii) defining the relevant  $N^2$  and  $(dT/dz)^2$ , and (iv) applying an iterative  
<sup>120</sup> method to compute  $\chi$  and  $K_T$ . We then discuss some limitations and practical considerations that  
<sup>121</sup> arise.

<sup>122</sup> *a. Iterative Method for estimating  $\chi$*

<sup>123</sup> For each  $\sim 1$  second window,  $\chi$  is estimated via the following procedure as outlined in Moum  
<sup>124</sup> and Nash (2009). For isotropic turbulence,

$$\chi_T = 6D_T \int_0^\infty \Psi_{T_x}(k) dk \quad (1)$$

125 where  $D_T$  is the thermal diffusivity and  $\Psi_{T_x}(k)$  is the wavenumber spectrum of  $dT/dx$ .

126 Note that  $dT/dx$  is not actually measured;  $dT/dt$  is measured, and  $dT/dx$  is inferred from

127 Taylor's frozen flow hypothesis:

$$\frac{dT}{dx} = \frac{1}{u} \frac{dT}{dt} \quad (2)$$

128 The wavenumber extent of the spectrum depends on the Batchelor wavenumber  $k_b$ , which is  
129 related to  $\varepsilon$ :

$$k_b = [\varepsilon / (v D_T^2)]^{1/4} \quad (3)$$

130 We assume that  $K_\rho = K_T$  and  $K_\rho = \Gamma \varepsilon / N^2$ . Then dissipation rate is computed as

$$\varepsilon_\chi = \frac{N^2 \chi_T}{2\Gamma \langle dT/dz \rangle^2} \quad (4)$$

131 Typical thermistors do not resolve the spectrum out to  $k_b$ , so the measured spectrum is fit to the  
132 Kraichnan form of theoretical scalar spectrum over the range of resolved wavenumbers ( $k_{min} <$   
133  $k < k_{max}$ ). The variance between the measured  $[\Phi_{T_x}(k)]_{obs}$  and theoretical  $[\Phi_{T_x}(k)]_{theory}$  spectra at  
134 these wavenumbers is assumed to be equal:

$$\int_{k_{min}}^{k_{max}} [\Phi_{T_x}(k)]_{obs} dk = \int_{k_{min}}^{k_{max}} [\Phi_{T_x}(k)]_{theory} dk \quad (5)$$

135 An iterative procedure is then used to fit and calculate  $\chi$  and  $\varepsilon$ :

136 1. First we estimate  $\chi_T$  based on an initial guess of  $\varepsilon = 10^{-7}$  Wkg $^{-1}$  and compute  $k_b$  via eq. 3.

137 We set  $k_{max} = k_b/2$  or to a wavenumber equivalent to  $f_{max} = 7$  Hz [i.e.,  $k_{max} = 2\pi(f_{max})/u$ ],  
138 whichever is smaller. We choose  $f_{max} = 7$  Hz because the thermistors' response rolls off at  
139 higher frequencies (see appendix for more details).

140 2. We then use Eq. (4) to refine our estimate of  $k_b$  and recompute  $\chi_T$  using Eqs. (1) and (5).

141 3. This sequence is repeated and converges after two or three iterations.

<sup>142</sup> Note that this procedure is equivalent to the explicit formulation of (Alford and Pinkel 2000),  
<sup>143</sup> except we use the Kraichnan theoretical form instead of the Batchelor spectrum for  $[\Phi_{T_x}(k)]_{theory}$ .

<sup>144</sup> b. CTD- $\chi$ pod Data Processing

<sup>145</sup> The basic outline for processing each CTD- $\chi$ -pod profile is as follows:

<sup>146</sup> 1. The correct time-offset for the  $\chi$ -pod clock is determined by aligning  $dp/dt$  from the 24Hz  
<sup>147</sup> CTD data to vertical velocity calculated by integrating vertical accelerations measured by the  
<sup>148</sup>  $\chi$ -pod.  $\chi$ -pod clock drift is small, typically on the order of 1 sec/week, but it is imperative to  
<sup>149</sup> get records aligned within  $< 0.5$  s so that the correct  $u = w = dp/dt$  is used.

<sup>150</sup> 2. Low-order polynomial calibration coefficients are determined to convert thermistor voltages  
<sup>151</sup> from  $\chi$ pod to ITS90 temperature (as measured by the CTD). Figure 3 shows an example of  
<sup>152</sup> the aligned and calibrated CTD- $\chi$ pod timeseries for one cast. Note the significant differences  
<sup>153</sup> in amount of variance associated with the two sensors during down and up casts. For the  
<sup>154</sup> upward-mounted sensor (T1), the downcast signal is associated with the CTD wake, as is the  
<sup>155</sup> upcast for the downward-mounted sensor (T2). Only the ‘clean’ portions of the cast (e.g., the  
<sup>156</sup> T1 upcast and the T2 downcast) are used in the  $\chi$ pod calculations.

<sup>157</sup> 3. Depth loops are identified and flagged in the 24Hz CTD data.  $\chi$ -pod data during these times  
<sup>158</sup> are discarded since the signals are likely contaminated by the wake of the CTD. Even for  
<sup>159</sup> profiles that are significantly affected by ship heaving, good segments of data are obtained  
<sup>160</sup> over a majority of the depths after removing contaminated data. JN: Include figure here. Also  
<sup>161</sup> include the criterion for identifying loops.

162 4. Buoyancy frequency  $N^2$  and temperature gradient  $dT/dz$  are computed from 1-m binned  
163 CTD data, and averaged over a scale of 10m. The results are not very sensitive to the averaging  
164 interval (see appendix for more details).

165 5. Half-overlapping 1 sec windows of data are used to estimate  $\chi$ ,  $\varepsilon$ , and  $K_T$  following the  
166 methods described in Moum and Nash (2009), as outlined in the previous section.

167 *c. Example Spectra and Fits*

168 Examples of the observed and fit spectra are shown in Figure 4, for low and high dissipation  
169 rate. Note that at lower  $\varepsilon$ , a larger fraction of  $k_b$  is observed and the peak of the spectrum is nearly  
170 resolved. At higher  $\varepsilon$ , less of the spectrum is resolved and the spectral peak is well above the  
171 maximum resolved wavenumber. Even so, the iterative  $\chi$ -pod method gives an accurate estimate  
172 of  $\chi$ . Also note that errors in  $\varepsilon$  can be larger, even when  $\chi$  is accurate; the shape of the spectrum  
173 at resolved wavenumbers is not sensitive to  $\varepsilon$ ?

174 *d. flowspeed past the sensor*

175 The flowspeed past the thermistor is needed to convert the measured temperature derivative  
176  $dT/dt$  to a spatial gradient. For the CTD- $\chi$ -pod, the largest contribution to the flowspeed is usually  
177 the vertical velocity of the CTD package ( $dp/dt$ ), which is close to 1m/s on average, so we typ-  
178 ically neglect the horizontal component of velocity in converting from frequency to wavenumber  
179 spectra. Although this will be a good approximation, errors may be introduced where horizontal  
180 velocities are large. Note that because it is the total instantaneous velocity magnitude that repre-  
181 sents flow past the sensor, neglecting the horizontal component of velocity (assuming  $u = dp/dt$ )  
182 means we are always underestimating the true flowspeed past the sensor. When the CTD package  
183 is equipped with LADCP, the true flowspeed can be measured. In some cases (including EQ14)

184 where the CTD was not equipped with LADCP, it would seem that the ship's ADCP could be  
185 used to estimate the horizontal component of velocity. However, because the CTD does not travel  
186 perfectly vertically in strong currents, this is difficult to do in practice. In a strong horizontal flow,  
187 the CTD will drift with the current while descending, lowering the flow relative to the sensors.  
188 On the upcasts, the CTD will be pulled against the current, increasing the flow relative to the sen-  
189 sors. Since the CTD in EQ14 was not equipped with LADCP, we use  $dp/dt$  as the flowspeed, and  
190 estimate potential errors in the appendix.

## 191 4. Results

### 192 a. Direct Test of $\chi$ pod Method

193 We begin by utilizing the highly-resolved turbulence profiler data (for which both  $\varepsilon$  and  $\chi$  are  
194 measured) to test the assumptions in our method of estimating  $\chi$ . We first apply the  $\chi$ pod method  
195 to each Chameleon profile, using only the FP07 thermistor data. These results, which we will refer  
196 to as  $\chi_\chi$ , are then compared with  $\chi_\varepsilon$ , computed by integrating the theoretical temperature gradient  
197 spectrum with  $k_b$  computed directly from shear-probe derived  $\varepsilon$ . Qualitatively,  $\chi_\chi$  and  $\chi_\varepsilon$  show  
198 very similar depth and time patterns (Figure 5), suggesting the method generally works well. A  
199 more quantitative comparison is made with a 2-D histogram (Figure 6), which shows that the two  
200 are well-correlated over a wide range of magnitudes.

### 201 b. CTD $\chi$ -pod - Chameleon Comparison

202 Having demonstrated that the method works for Chameleon data, we now compare  $\chi$  from CTD-  
203 mounted  $\chi$ pods to  $\chi_\varepsilon$ . In contrast to the Chameleon data, the CTD is more strongly coupled to  
204 the ship, and therefore subject to more vibration, heaving, and artificial turbulence created by the  
205 rosette. A total of 35 CTD- $\chi$ pod casts were done with Chameleon profiles immediately before and

206 after. We first compare CTD- $\chi$ pod profiles to the mean of the two Chameleon profiles bracketing  
207 each cast, both averaged in 5m depth bins (Figure 8). The two are correlated, but with considerable  
208 scatter. However, we expect significant natural variability even between Chameleon profiles. Scat-  
209 ter plots of before vs. after Chameleon profiles (not shown), typically separated by about an hour,  
210 show a similar level of scatter as the differences between methods, suggesting that the observed  
211 differences (Figure 8) can be explained by natural variability in turbulence. This is demonstrated  
212 by histograms of the ratio of  $\chi$  from adjacent casts (Figure 9) which show that the variability be-  
213 tween CTD  $\chi$ pod and Chameleon casts is similar to the natural variability between before/after  
214 Chameleon profiles. Average profiles from all CTD-Chameleon pairs (Figure 10) overlap within  
215 95% confidence limits at all depths where there exists good data for both. Averages of subsets of  
216 profiles clustered in position/time (not shown) also agree well.

## 217 5. Discussion

218 We have shown that  $\chi$  can be accurately estimated from  $\chi$ pods attached to CTD rosettes. The  
219 method also estimates  $\varepsilon$ , but we have not discussed it here since it involves more assumptions  
220 and uncertainties. One major assumption is the mixing efficiency  $\Gamma$ . A value of 0.2 is commonly  
221 assumed, but evidence suggests this may vary significantly (see appendix for a study of the sensi-  
222 tivity to this parameter). The  $\chi$ pod method also assumes that  $K_T = K_\rho$ . Even if  $\varepsilon$  estimates have  
223 a large uncertainty,  $\chi$  and  $K_T$  are robust and should be useful to the community.

224 The goal of CTD- $\chi$ pods is to expand the number and spatial coverage of ocean mixing ob-  
225 servations. We have already deployed instruments during several experiments (IWISE, TTIDE)  
226 and on several GO-SHIP repeat-hydrography cruises. We plan to continue regular deployment on  
227 GO-SHIP and similar cruises, adding  $\chi$  and  $K_T$  to the suite of variables measured and enabling  
228 scientists to explore relationships between these and other variables. The expanding database of

229 mixing measurements from CTD- $\chi$ pods will also enable testing of other commonly-used or new  
230 mixing parameterizations. An example of data from a portion of the P16 GO-SHIP cruise is shown  
231 in Figure 11.

## 232 6. Conclusions

- 233 • The  $\chi$ pod method for estimating  $\chi$  and  $K_T$  was directly applied to temperature gradients  
234 measured by the Chameleon microstructure profiler on > 2700 profiles during the EQ14  
235 cruises. The estimated  $\chi_\chi$  agrees well with  $\chi_e$  calculated using  $\varepsilon$  from shear probes over a  
236 wide range of magnitudes (Figure 6), demonstrating that the method works.
- 237 • CTD- $\chi$ pod profiles were also compared to nearby Chameleon profiles during the cruise. Vari-  
238 ability between CTD- $\chi$ pod and Chameleon estimates of  $\chi$  is similar to natural variability  
239 between Chameleon profiles. Time-averaged profiles of  $\chi$  from both platforms agree within  
240 95% confidence limits, and no significant bias was detected between the estimates of  $\chi$ .
- 241 • We conclude that estimates of  $\chi$  and  $K_T$  made from the CTD- $\chi$ pod platform are robust and  
242 reliable.

243 *Acknowledgments.* The EQ14 experiment was funded by ??. We thank the Captain and crew of  
244 R/V Oceanus. Also thank people who helped collect the data, those who made the sensors, etc..

## 245 APPENDIX A

### 246 Sensitivity Analysis

#### 247 A1. Flowspeed Past Sensor

248 We investigate the sensitivity of the  $\chi$ pod calculations to flowspeed, which is used to convert  
249 temperate gradient spectra from the frequency domain to the wavenumber domain via Taylor's

250 frozen flow hypothesis. In this data, we have ignored any horizontal velocities and assumed the  
251 flow speed is equal to the vertical speed of the CTD rosette, determined from the recorded pressure  
252  $dp/dt$ . To test the sensitivity of the  $\chi$  pod method to flowspeed, we repeated the calculations with  
253 constant offsets added to the flowspeed. Since the total magnitude of velocity is used,  $dp/dt$   
254 is a minimum estimate of the true speed. Adding 0.1(1)m/s results in a median error of 13(52)  
255 percent (Figure 12). Increasing the velocity tends to result in smaller values of  $\chi$ , since it shifts  
256 the spectrum to lower wavenumbers.

257 We also looked for any biases associated with flowpseed. We found the  $\chi$  was biased high for  
258 very small speeds ( $u < 25\text{cm/s}$ ). This could be assoicated with contamination by CTD wake or  
259 entrained water when the CTD slows. We discard these values in our analysis.

260 **A2.  $N^2$  and  $dT/dz$**

261 We investigated the sensitivity of the calculations to the scale over which  $N^2$ ,  $dT/dz$  are aver-  
262 aged. The iterative method to estimate chi requires the background stratification  $N^2$  and tempera-  
263 ture gradient  $dT/dz$ . The estimate of  $\chi$  is insenstive to these scales. However, while dissipation  
264 rate  $\varepsilon$  and diffusivity  $K_T$  are more strongly affected because they are linearly related to these val-  
265 ues. Computing  $N^2$  and  $dT/dz$  over smaller scales results in larger values and hence some larger  
266 values of  $K_T$ .

267 **A3. Mixing Efficiency**

268 We also examined the sensitivity to the value of the mixing efficiency  $\Gamma$ . A value of 0.2 is  
269 commonly assumed, although several studies have indicated it could be different or variable. We  
270 used several values and compared each to the reference case of  $\Gamma = 0.2$ . Values of  $\chi$  ranged up to  
271  $\pm 2$  times the reference values.

272

## APPENDIX B

273

### Test of MLE fitting method

274 We tested the spectrum fitting method of Ruddick et al. (2000) and found that this method does  
 275 not work well for the  $\chi$  pod data, where only a small fraction of the spectrum is resolved. In  
 276 particular, the MLE method underestimates  $\chi$  at larger magnitudes (Figure 13). At lower profiling  
 277 speeds we would expect the MLE method to work better, as more of the spectrum will be resolved.

278

## APPENDIX D

279

### Thermistor Frequency Response

280 Prior to 2009, the transfer function for each FP07 thermistor was measured by profiling next to a  
 281 thermocouple? in Yaquina Bay, OR. However, measuring the transfer function for each individual  
 282 thermistor proved too expensive and time-consuming, and since that time a generic transfer func-  
 283 tion has been used. Figure 14 shows the measured transfer functions for 2008. The majority of the  
 284 the transfer functions are similar for at frequencies up to about 10 Hz, and begin to significantly  
 285 differ above that. To estimate the potential error in not using a transfer function, we calculated the  
 286 % of spectral variance captured for each of the measured functions (Fig 15). For frequencies up to  
 287 7Hz, more than 90% is captured for the majority of the measured functions. We also found that us-  
 288 ing only frequencies up to 7Hz (where the transfer function is equal to or very close to unity) gave  
 289 good agreement with the Chameleon data, and avoids the issue of the unknown transfer functions.

290

### References

291 Alford, M., and R. Pinkel, 2000: Patterns of turbulent and double diffusive phenomena: Observa-  
 292 tions from a rapid profiling conductivity probe. *J. Phys. Oceanogr.*, **30**, 833–854.

- 293 Bachelor, G. K., 1959: Small-scale variation of convected quantitites like temperature in turbulent  
294 fluid. *J. Fluid Mech.*, **5**, 113–139.
- 295 Dillon, T. M., 1982: Vertical overturns: A comparison of Thorpe and Ozmidov length scales. *J.*  
296 *Geophys. Res.*, **87**, 9601–9613.
- 297 Galbraith, P. S., and D. E. Kelley, 1996: Identifying overturns in CTD profiles. *J. Atmos. Ocean.*  
298 *Tech.*, **13**, 688–702.
- 299 Gregg, M., 1989: Scaling turbulent dissipation in the thermocline. *J. Geophys. Res.*, **94 (C7)**,  
300 9686–9698.
- 301 Kunze, E., E. Firing, J. Hummon, T. K. Chereskin, and A. Thurnherr, 2006: Global abyssal mixing  
302 inferred from lowered ADCP shear and CTD strain profiles. *Journal of Physical Oceanography*,  
303 **36 (8)**, 1553–1576.
- 304 Mater, B. D., S. K. Venayagamoorthy, L. S. Laurent, and J. N. Moum, 2015: Biases in Thorpe scale  
305 estimates of turbulence dissipation Part I: Assessments from large-scale overturns in oceanographic  
306 data. *J. Phys. Oceanogr.*, **45 (2015)**, 2497–2521.
- 307 Melet, A., R. Hallberg, S. Legg, and K. L. Polzin, 2013: Sensitivity of the ocean state to the  
308 vertical distribution of internal-tide-driven mixing. *J. Phys. Oceanogr.*, **43 (3)**, 602–615, doi:  
309 <http://dx.doi.org/10.1175/JPO-D-12-055.1>.
- 310 Moum, J., and J. Nash, 2009: Mixing measurements on an equatorial ocean mooring. *J. Atmos.*  
311 *Ocean. Tech.*, **26**, 317–336.
- 312 Munk, W., and C. Wunsch, 1998: Abyssal recipes II: energetics of tidal and wind mixing. *Deep-*  
313 *Sea Res. Part I*, **45**, 1977–2010.

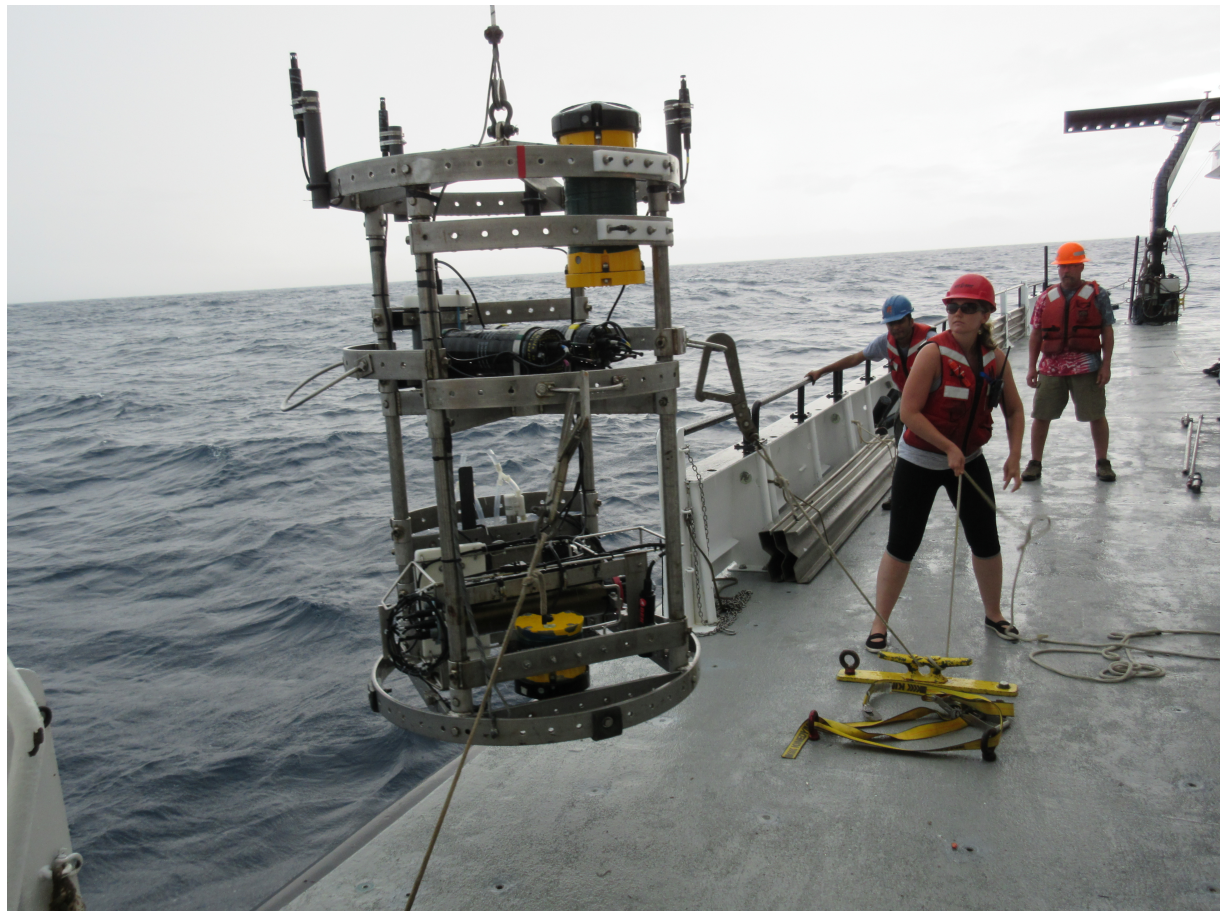
- <sup>314</sup> Munk, W. H., 1966: Abyssal recipes. *Deep-Sea Res.*, **13**, 707–730.
- <sup>315</sup> Osborn, T. R., 1980: Estimates of the local rate of vertical diffusion from dissipation measurements. *J. Phys. Oceanogr.*, **10**, 83–89.
- <sup>316</sup>
- <sup>317</sup> Osborn, T. R., and C. S. Cox, 1972: Oceanic fine structure. *Geophys. Fluid Dyn.*, **3**, 321–345.
- <sup>318</sup> Polzin, K. L., A. C. Naveira Garabato, T. N. Huussen, B. M. Sloyan, and S. N. Waterman, 2013:
- <sup>319</sup> Finescale parameterizations of turbulent dissipation. *Rev. Geophys.*, **submitted**.
- <sup>320</sup> Ruddick, B., A. Anis, and K. Thompson, 2000: Maximum likelihood spectral fitting: The Batch-
- <sup>321</sup> elor spectrum. *J. Atmos. Ocean. Tech.*, **17**, 1541–1555.
- <sup>322</sup> Scotti, A., 2015: Biases in Thorpe scale estimates of turbulence dissipation Part II: Energetics
- <sup>323</sup> arguments and turbulence simulations. *J. Phys. Oceanogr.*, **45 (2015)**, 2522–2543.
- <sup>324</sup> Thorpe, S., 1977: Turbulence and mixing in a Scottish Loch. *Philos. Trans. R. Soc. London Ser.*
- <sup>325</sup> *A*, **286**, 125–181.
- <sup>326</sup> Waterhouse, A. F., and Coauthors, 2014: Global patterns of diapycnal mixing from measurements
- <sup>327</sup> of the turbulent dissipation rate. *J. Phys. Oceanogr.*, **44 (7)**, 1854–1872.
- <sup>328</sup> Waterman, S., A. C. N. Garabato, and K. L. Polzin, 2013: Internal waves and turbulence in the
- <sup>329</sup> antarctic circumpolar current. *Journal of Physical Oceanography*, **43 (2)**, 259–282.
- <sup>330</sup> Whalen, C. B., J. A. MacKinnon, L. D. Talley, and A. F. Waterhouse, 2015: Estimating the
- <sup>331</sup> mean diapycnal mixing using a finescale strain parameterization. *Journal of Physical Oceanog-*
- <sup>332</sup> *rphy*, **45 (4)**, 1174–1188, doi:10.1175/JPO-D-14-0167.1, URL <http://dx.doi.org/10.1175/JPO-D-14-0167.1>.
- <sup>333</sup>

<sup>334</sup> Whalen, C. B., L. D. Talley, and J. A. MacKinnon, 2012: Spatial and temporal variabil-  
<sup>335</sup> ity of global ocean mixing inferred from argo profiles. *Geophys. Res. Lett.*, **39** (L18612),  
<sup>336</sup> doi:10.1029/2012GL053196.

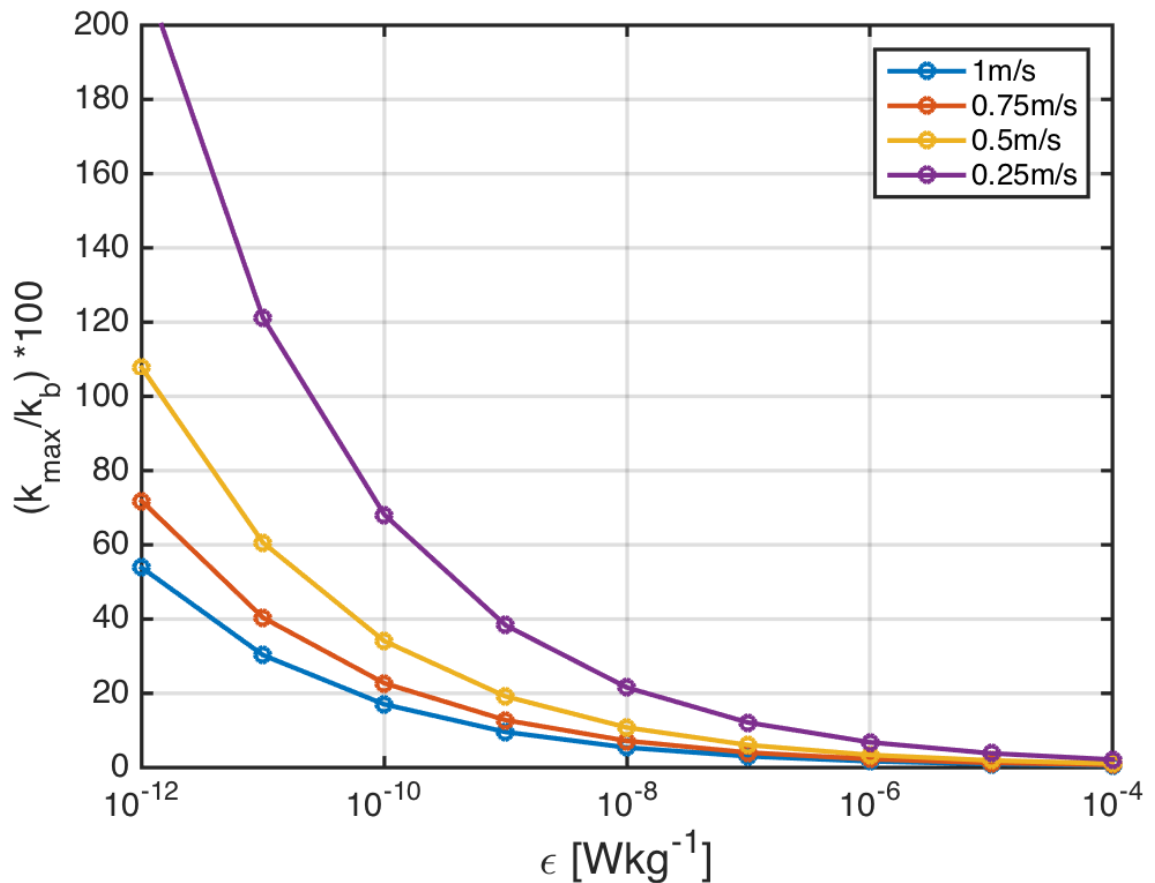
## 337 LIST OF FIGURES

338	<b>Fig. 1.</b> Photo of CTD rosette during EQ14 with $\chi$ -pods attached. ** Add close-up picture of mini-	20
339	chipod unit too**	
340	<b>Fig. 2.</b> Ratio of the maximum observed wavenumber $k_{max} = f_{max}/u$ to the Batchelor wavenumber	21
341	$k_b$ for different values of $\varepsilon$ , assuming a $f_{max} = 7Hz$ . Each line is for a different flowspeed.	
342	<b>Fig. 3.</b> Example timeseries from one CTD cast during EQ14. a) CTD pressure. b) Fallspeed of	22
343	CTD ( $dp/dt$ ) .c) Vertical and horizontal accelerations measured by $\chi$ -pod. d) Temperature	
344	from CTD and (calibrated) $\chi$ -pod sensors. T2 is offset slightly for visualization. e) Temper-	
345	ature derivative $dT/dt$ measured by the upward-looking $\chi$ -pod sensor T1. f) Temperature	
346	derivative $dT/dt$ measured by the downward-looking $\chi$ -pod sensor T2. **calibrate,add AX	
347	units. is it really -dT/dt? add 'up/down' looking labels for T' panels.	
348	<b>Fig. 4.</b> Example temperature gradient spectra from EQ14, for high (top) and low (bottom) $\varepsilon$ . Solid	23
349	black line show the observed spectra. Dashed line shows the fitted theoretical Kraichnan	
350	spectra for the $\chi$ pod estimates. Magenta line is Kraichnan spectra for Chameleon $\chi$ and	
351	$\varepsilon$ . Vertical dashed blue lines indicate the minimum and maximum wavenumber used in the	
352	$\chi$ pod calculation. The Batchelor wavenumber $k_b$ is also indicated by the cyan line.	
353	<b>Fig. 5.</b> Depth-time plots of $\log_{10}\chi$ from both methods for EQ14 data. Top: $\chi$ pod method. Black	24
354	diamonds indicate casts used for comparison with CTD- $\chi$ pod profiles. Bottom: Chameleon.	
355	<b>Fig. 6.</b> 2D histogram of $\log_{10}(\chi)$ from Chameleon (x-axis) and $\chi$ pod method (y-axes). Values from	25
356	each profile were averaged in the same 5m depth bins.	
357	<b>Fig. 7.</b> Histogram of the (left) ratio of the maximum observed wavenumber $k_{max}$ to the Batchelor	26
358	wavenumber $k_b$ , and (right) fspd for all profiles in EQ14.	
359	<b>Fig. 8.</b> Scatter plot of $\chi$ from CTD- $\chi$ pod profiles versus the mean of bracketing Chameleon profiles.	27
360	Black dashed line shows 1:1, red are $\pm 10 X$ . **replace with histogram of ratios, or combine	
361	into one figure?**	
362	<b>Fig. 9.</b> Histogram of $\log_{10}$ of the ratio of $\chi$ for nearby casts. The first set is for the before	28
363	(cham1) and after (cham2) Chameleon profiles. the 2nd is CTD- $\chi$ pod profiles versus the	
364	before(cham1) profiles. The last is CTD- $\chi$ pod profiles versus the after(cham2) profiles.	
365	Dashed lines show the medians of each set. Note that bias is small/zero, and the variability	
366	(spread) between CTD/cham is similar to the natural variability between cham profiles.	
367	<b>Fig. 10.</b> Time mean of $\chi$ for all CTD- $\chi$ pod - Chameleon cast pairs, with 95% bootstrap confidence	29
368	intervals.	
369	<b>Fig. 11.</b> Example chipod data from P16N. Top: $dTdz$ . Bottom: $\chi$ .	30
370	<b>Fig. 12.</b> Histogram of % error for $\chi$ computed with constant added to fallspeed, in order to examine	31
371	sensitivity to fallspeed.	
372	<b>Fig. 13.</b> 2D histograms of $\chi$ computed using the interative $\chi$ -pod method (top) and the MLE fit	32
373	(bottom) versus $\chi$ computed from Chameleon. Note that the MLE method underestimates	
374	$\chi$ at larger magnitudes.	
375	<b>Fig. 14.</b> Measured FP07 thermistor transfer functions.	33

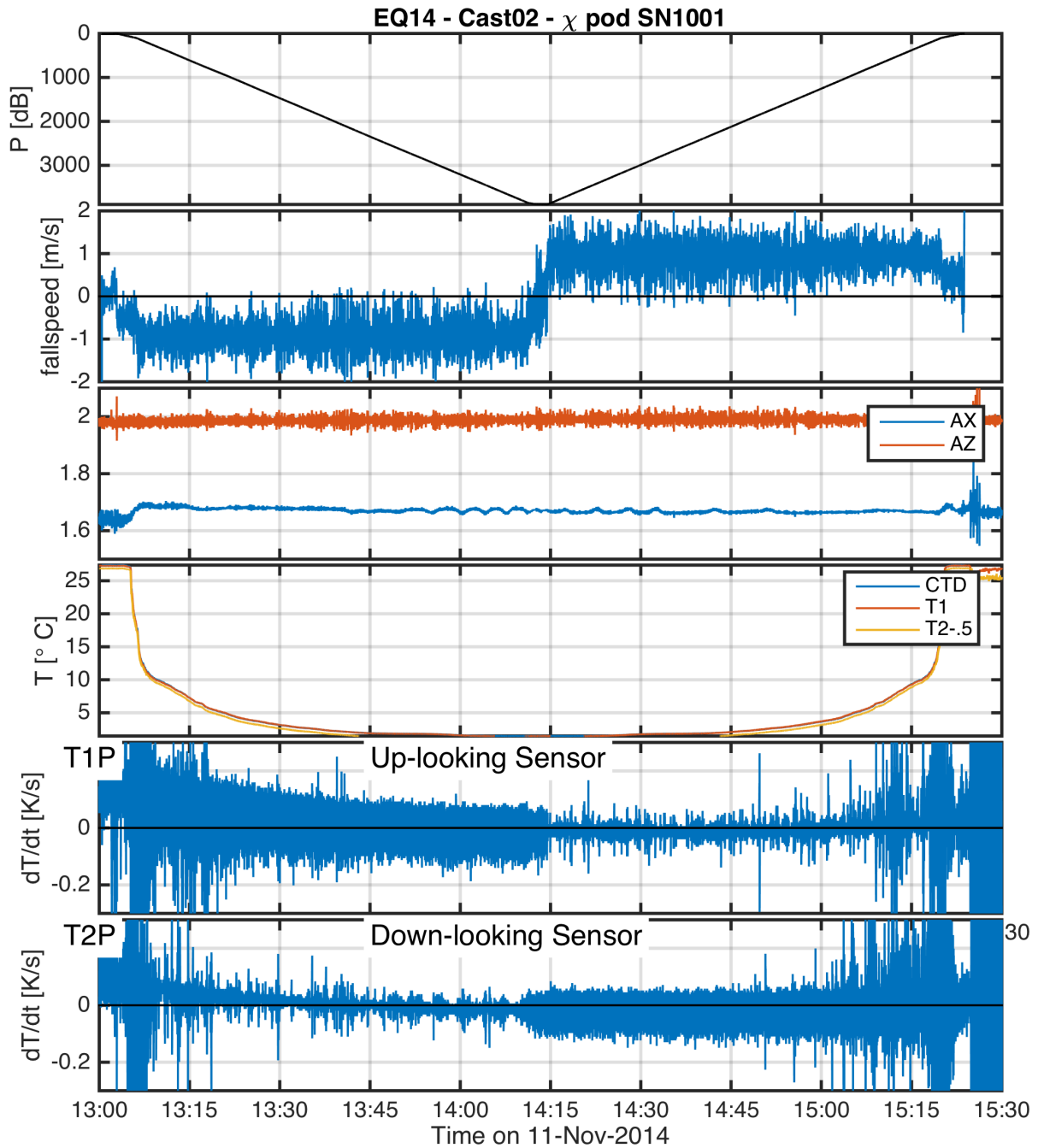
**Fig. 15.** Boxplots of the % variance of spectra captured using no transfer function over two different ranges of frequencies. Based on transfer functions in figure 14. . . . . 34



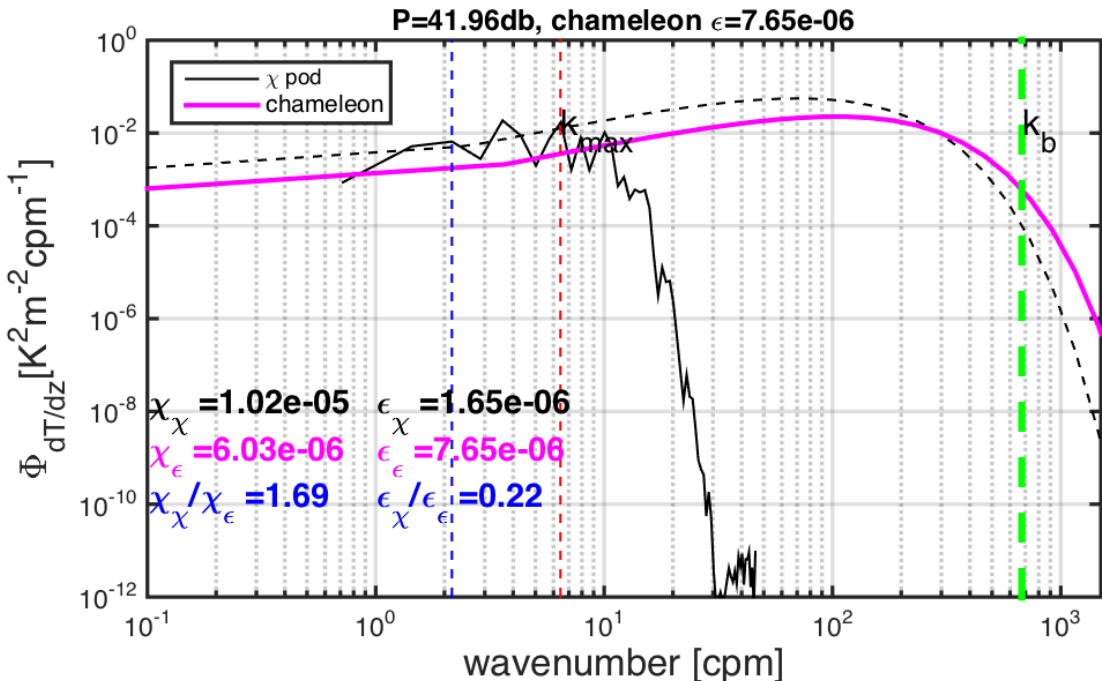
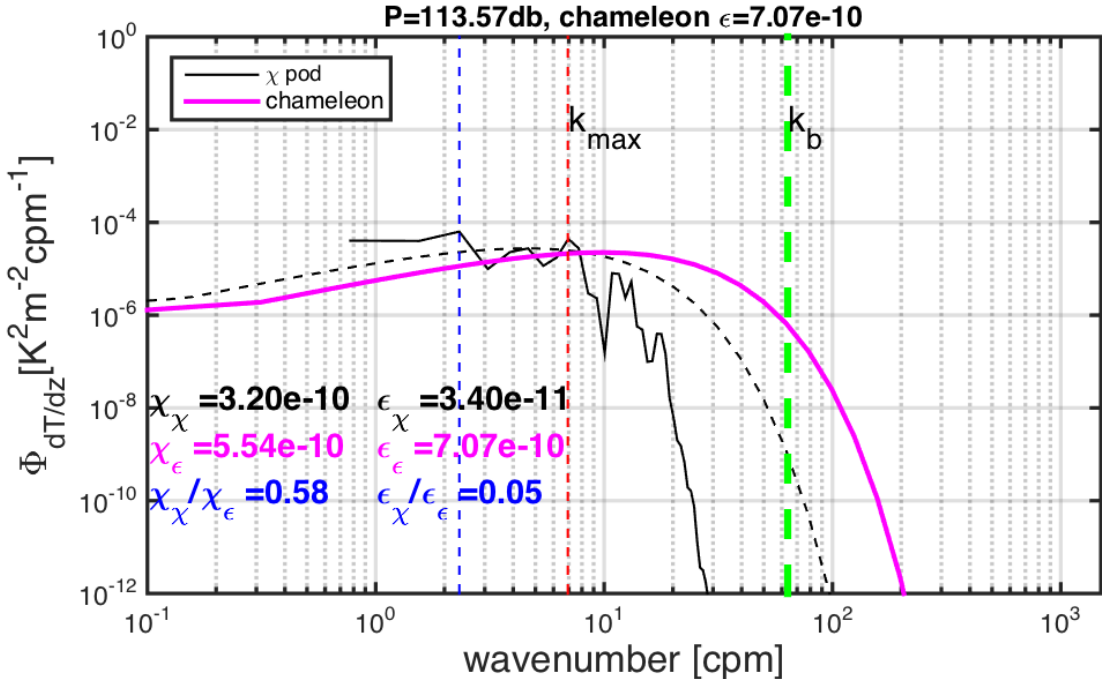
378 FIG. 1. Photo of CTD rosette during EQ14 with  $\chi$ -pods attached. \*\* Add close-up picture of mini-chipod  
379 unit too\*\*



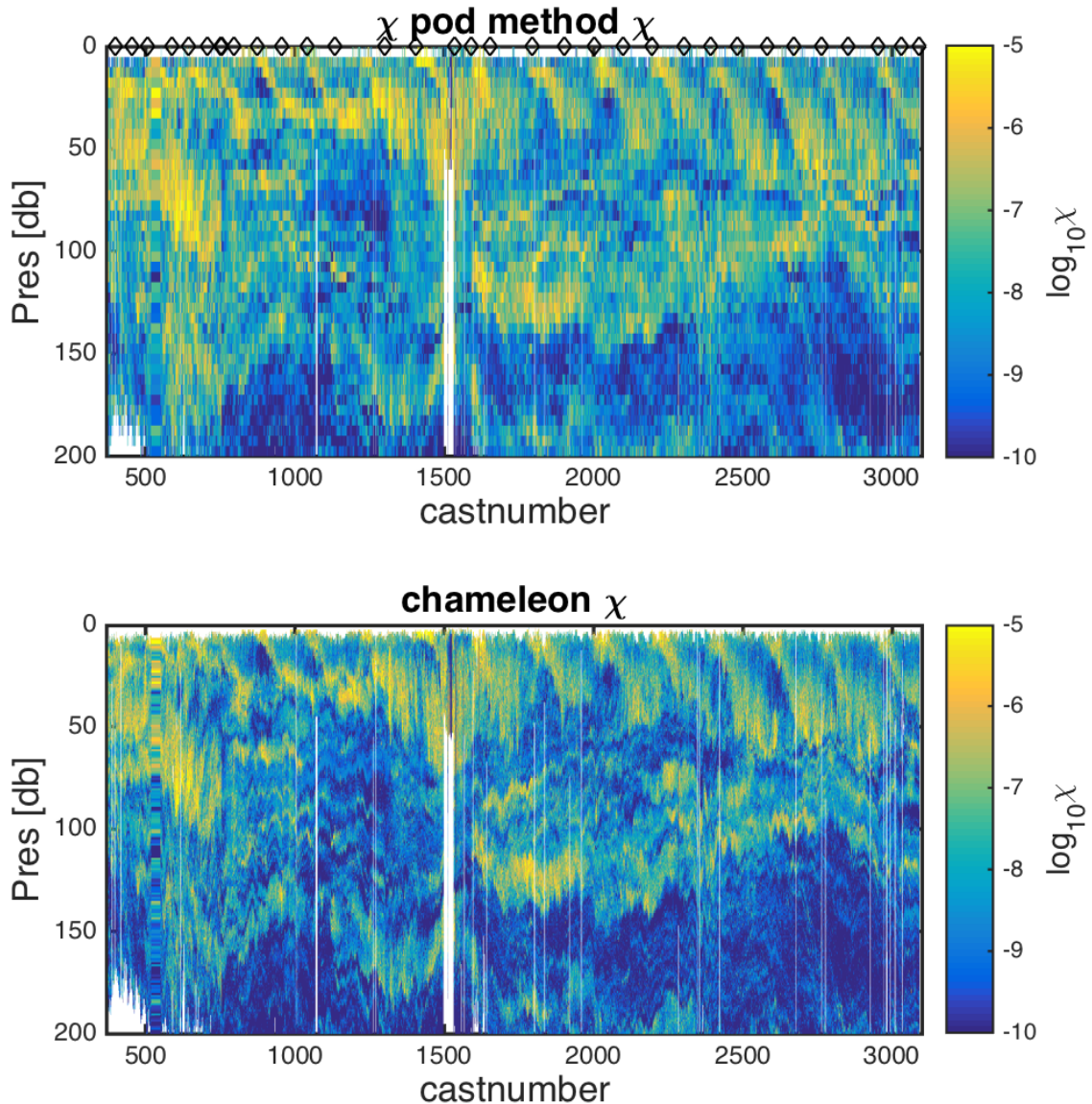
380 FIG. 2. Ratio of the maximum observed wavenumber  $k_{\max} = f_{\max}/u$  to the Bachelor wavenumber  $k_b$  for  
 381 different values of  $\epsilon$ , assuming a  $f_{\max} = 7\text{Hz}$ . Each line is for a different flowspeed.



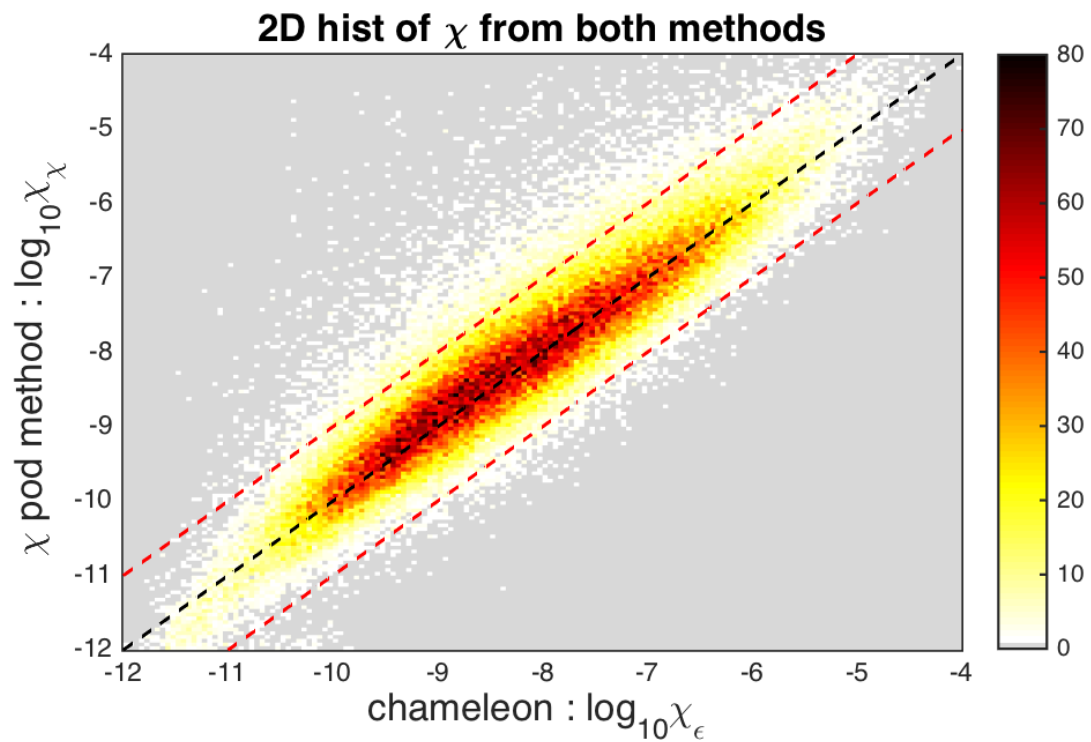
382 FIG. 3. Example timeseries from one CTD cast during EQ14. a) CTD pressure. b) Fallspeed of CTD ( $dp/dt$ )  
 383 .c) Vertical and horizontal accelerations measured by  $\chi$ -pod. d) Temperature from CTD and (calibrated)  $\chi$ -pod  
 384 sensors. T2 is offset slightly for visualization. e) Temperature derivative  $dT/dt$  measured by the upward-  
 385 looking  $\chi$ -pod sensor T1. f) Temperature derivative  $dT/dt$  measured by the downward-looking  $\chi$ -pod sensor  
 386 T2. \*\*calibrate,add AX units. is it really -dT/dt? add 'up/down' looking labels for T' panels.  
 23



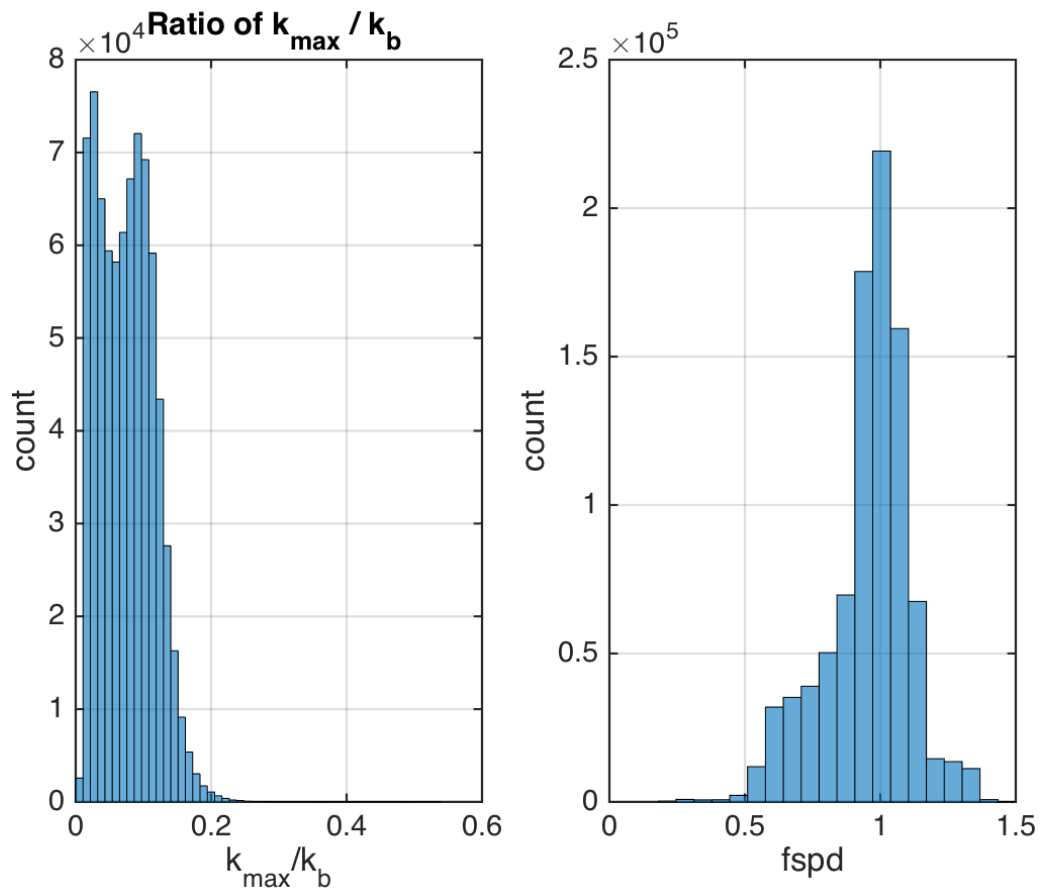
387 FIG. 4. Example temperature gradient spectra from EQ14, for high (top) and low (bottom)  $\epsilon$ . Solid black line  
 388 show the observed spectra. Dashed line shows the fitted theoretical Kraichnan spectra for the  $\chi$ pod estimates.  
 389 Magenta line is Kraichnan spectra for Chameleon  $\chi$  and  $\epsilon$ . Vertical dashed blue lines indicate the minimum and  
 390 maximum wavenumber used in the  $\chi$ pod calculation. The Batchelor wavenumber  $k_b$  is also indicated by the  
 391 cyan line.



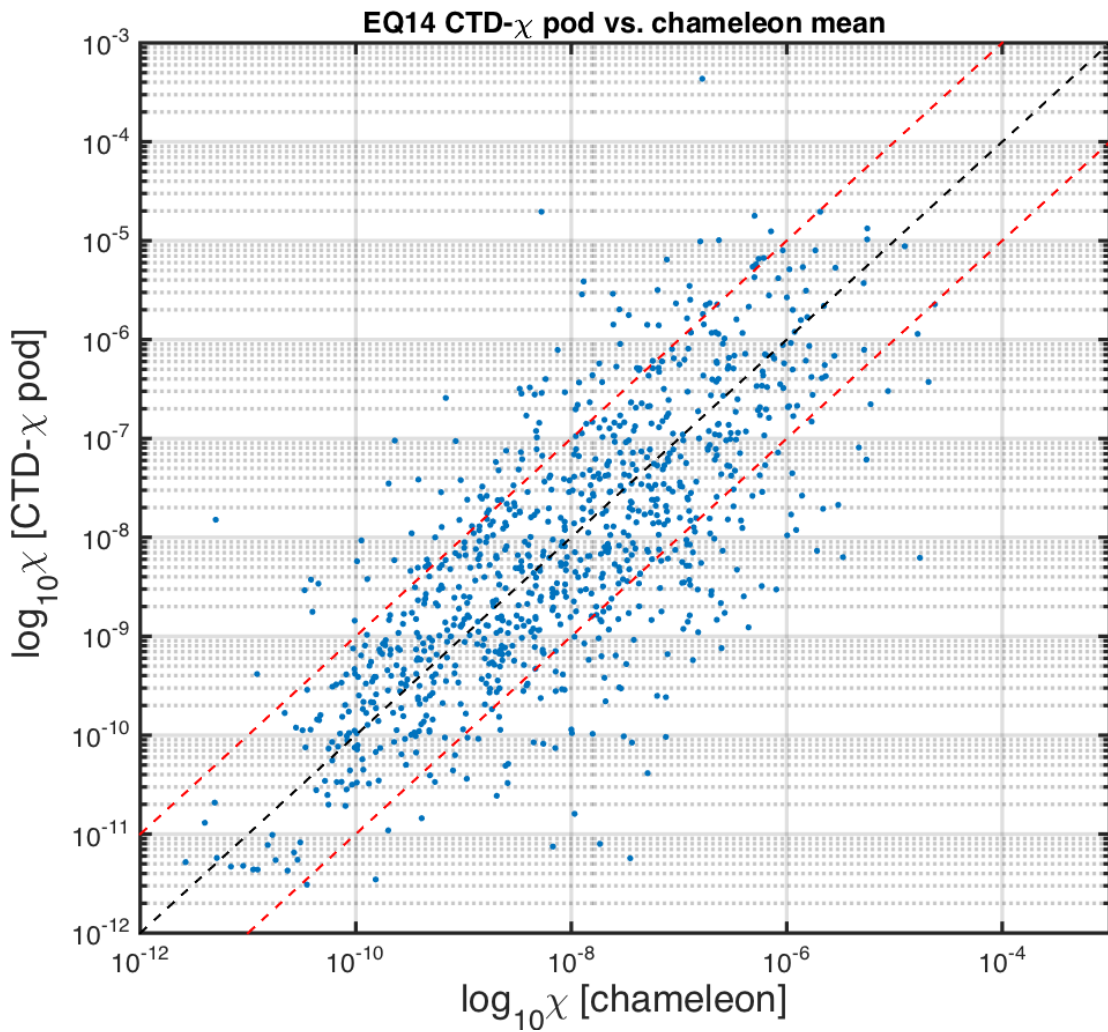
392 FIG. 5. Depth-time plots of  $\log_{10} \chi$  from both methods for EQ14 data. Top:  $\chi_{\text{pod}}$  method. Black diamonds  
 393 indicate casts used for comparison with CTD- $\chi_{\text{pod}}$  profiles. Bottom: Chameleon.



<sup>394</sup> FIG. 6. 2D histogram of  $\log_{10}(\chi)$  from Chameleon (x-axis) and  $\chi$  pod method (y-axes). Values from each  
<sup>395</sup> profile were averaged in the same 5m depth bins.



396 FIG. 7. Histogram of the (left) ratio of the maximum observed wavenumber  $k_{max}$  to the Bachelor wavenumber  
 397  $k_b$ , and (right) fspd for all profiles in EQ14.



<sup>398</sup> FIG. 8. Scatter plot of  $\chi$  from CTD- $\chi$  pod profiles versus the mean of bracketing Chameleon profiles. Black  
<sup>399</sup> dashed line shows 1:1, red are  $\pm 10 \times$ . \*\*replace with histogram of ratios, or combine into one figure?\*\*

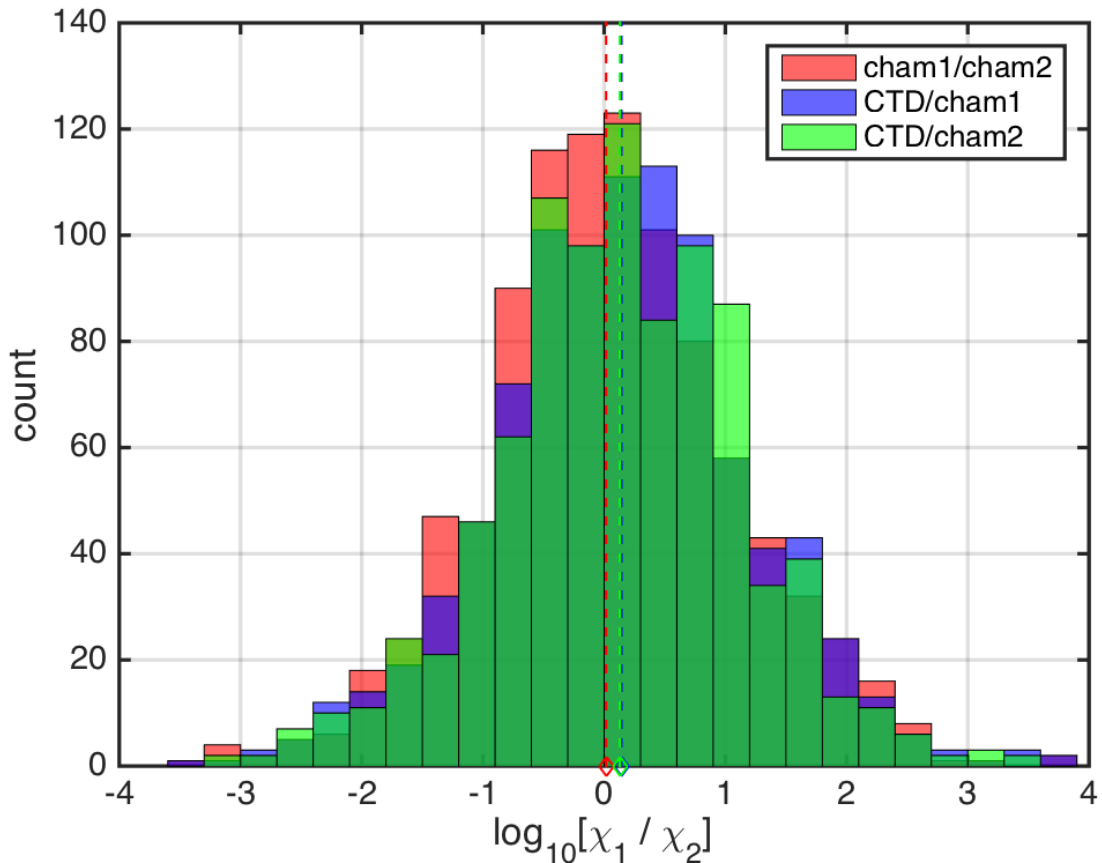


FIG. 9. Histogram of  $\log_{10}$  of the ratio of  $\chi$  for nearby casts. The first set is for the before (cham1) and after (cham2) Chameleon profiles. the 2nd is CTD- $\chi$ pod profiles versus the before(cham1) profiles. The last is CTD- $\chi$ pod profiles versus the after(cham2) profiles. Dashed lines show the medians of each set. Note that bias is small/zero, and the variability (spread) between CTD/cham is similar to the natural variability between cham profiles.

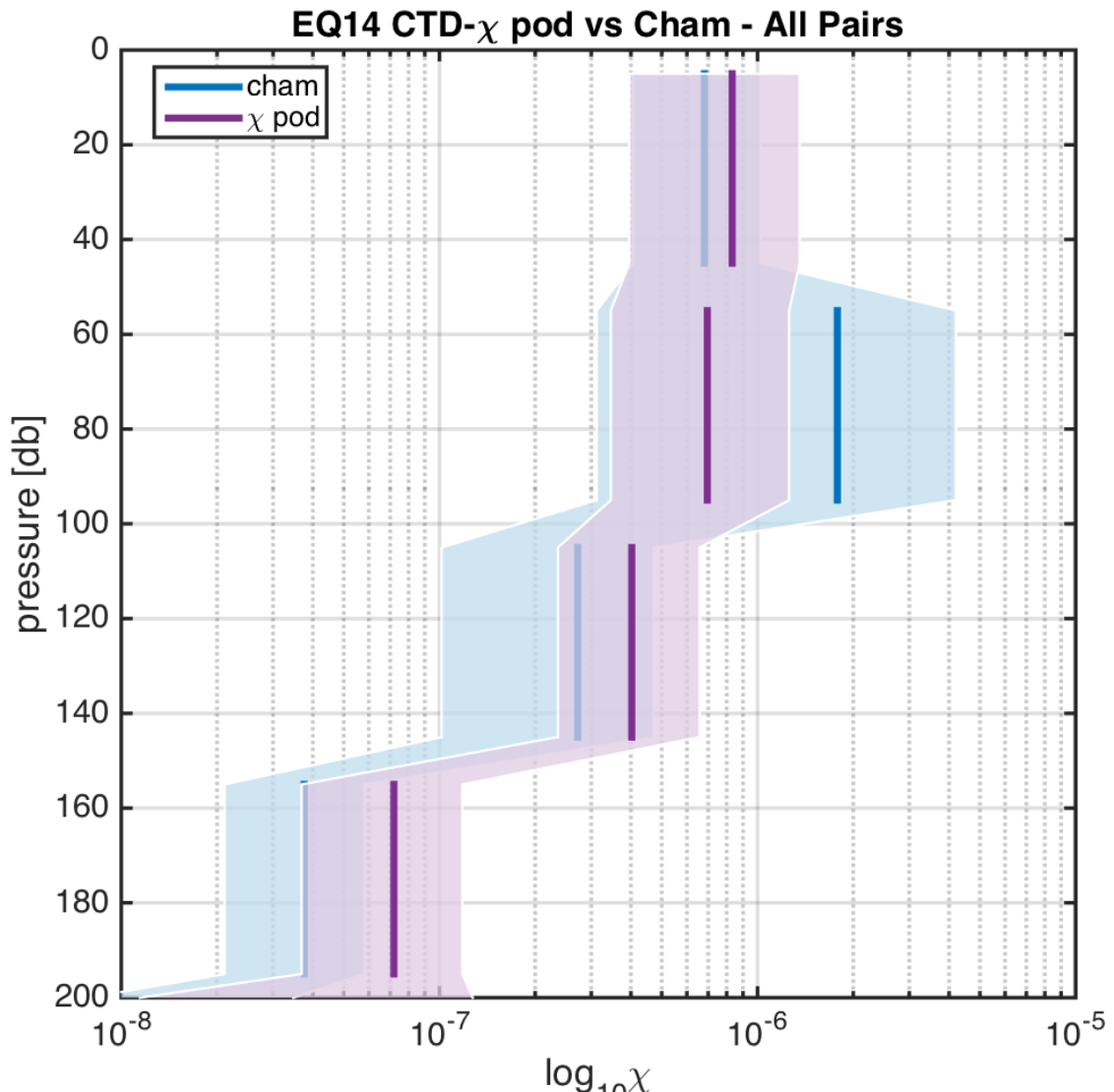


FIG. 10. Time mean of  $\chi$  for all CTD- $\chi$  pod - Chameleon cast pairs, with 95% bootstrap confidence intervals.

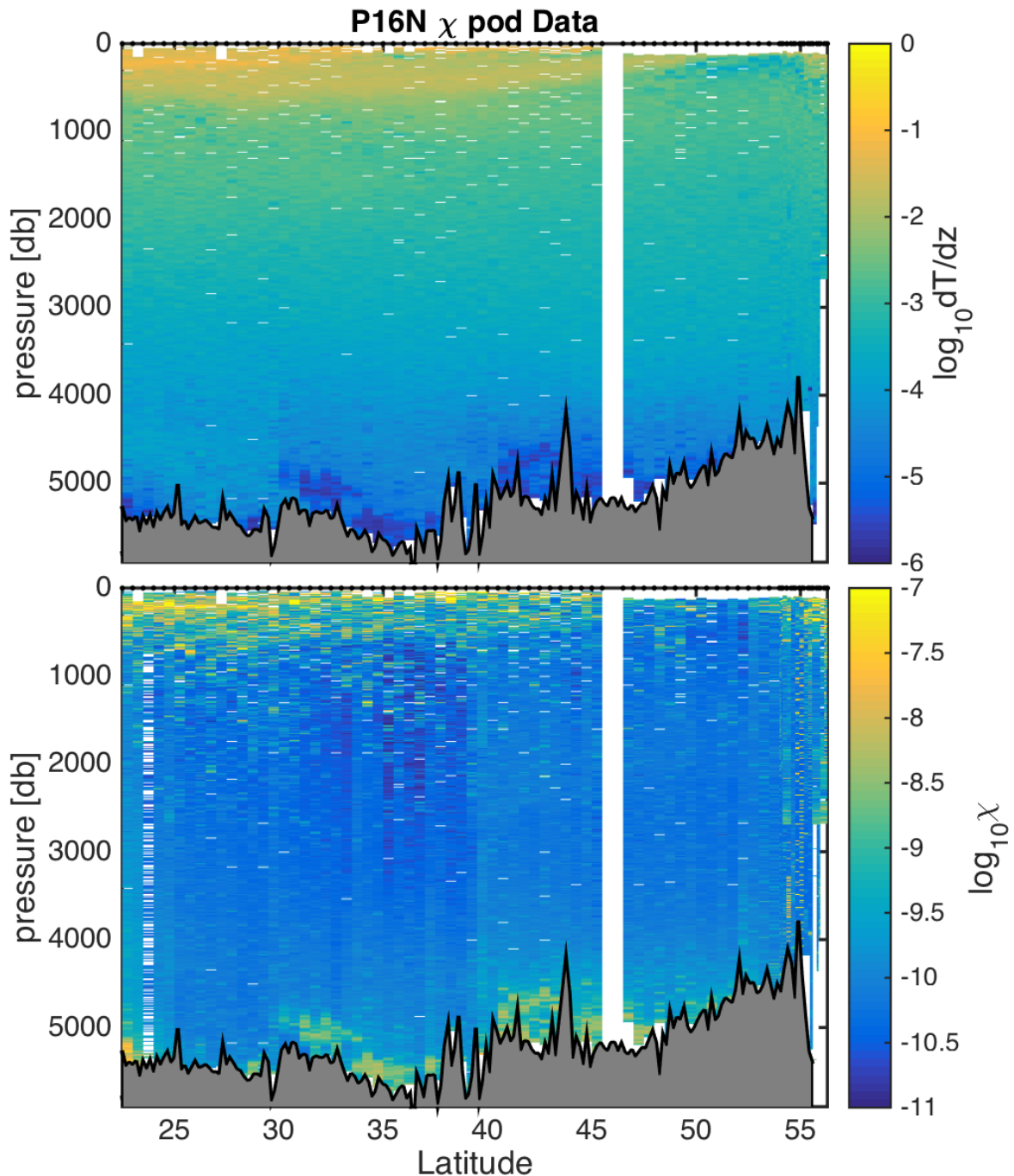
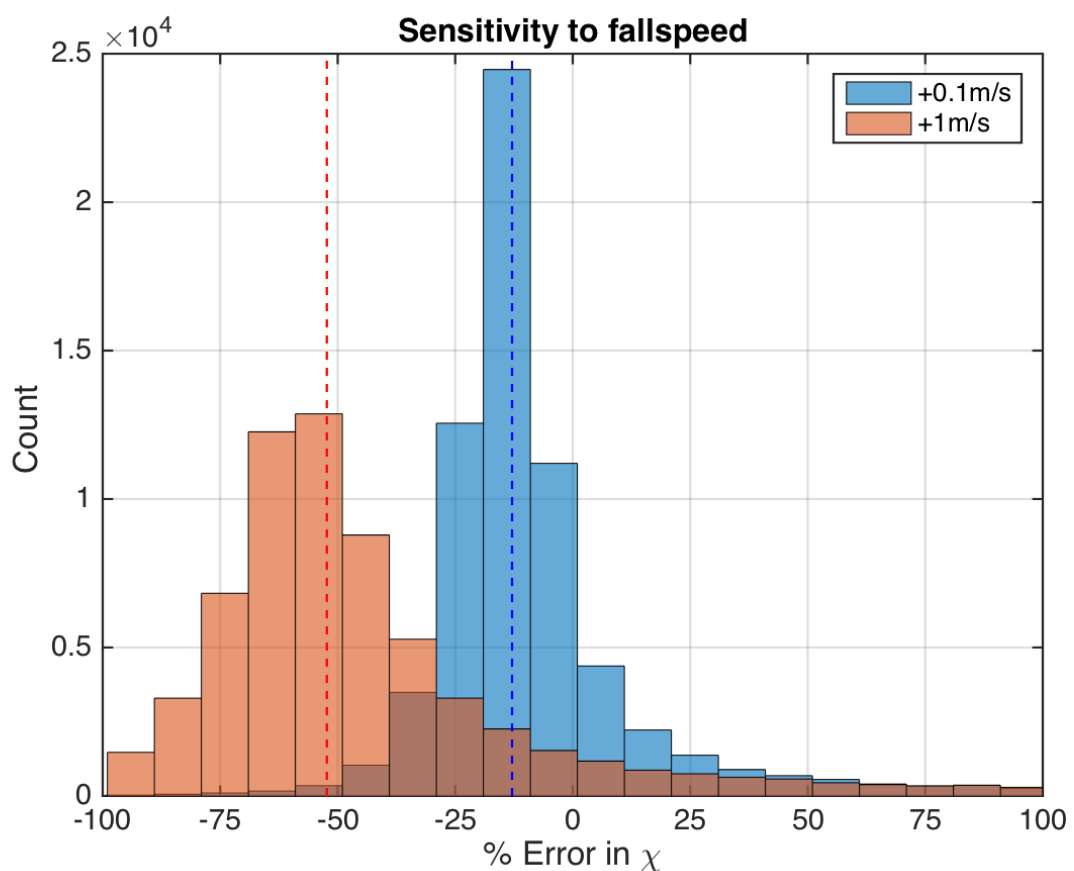
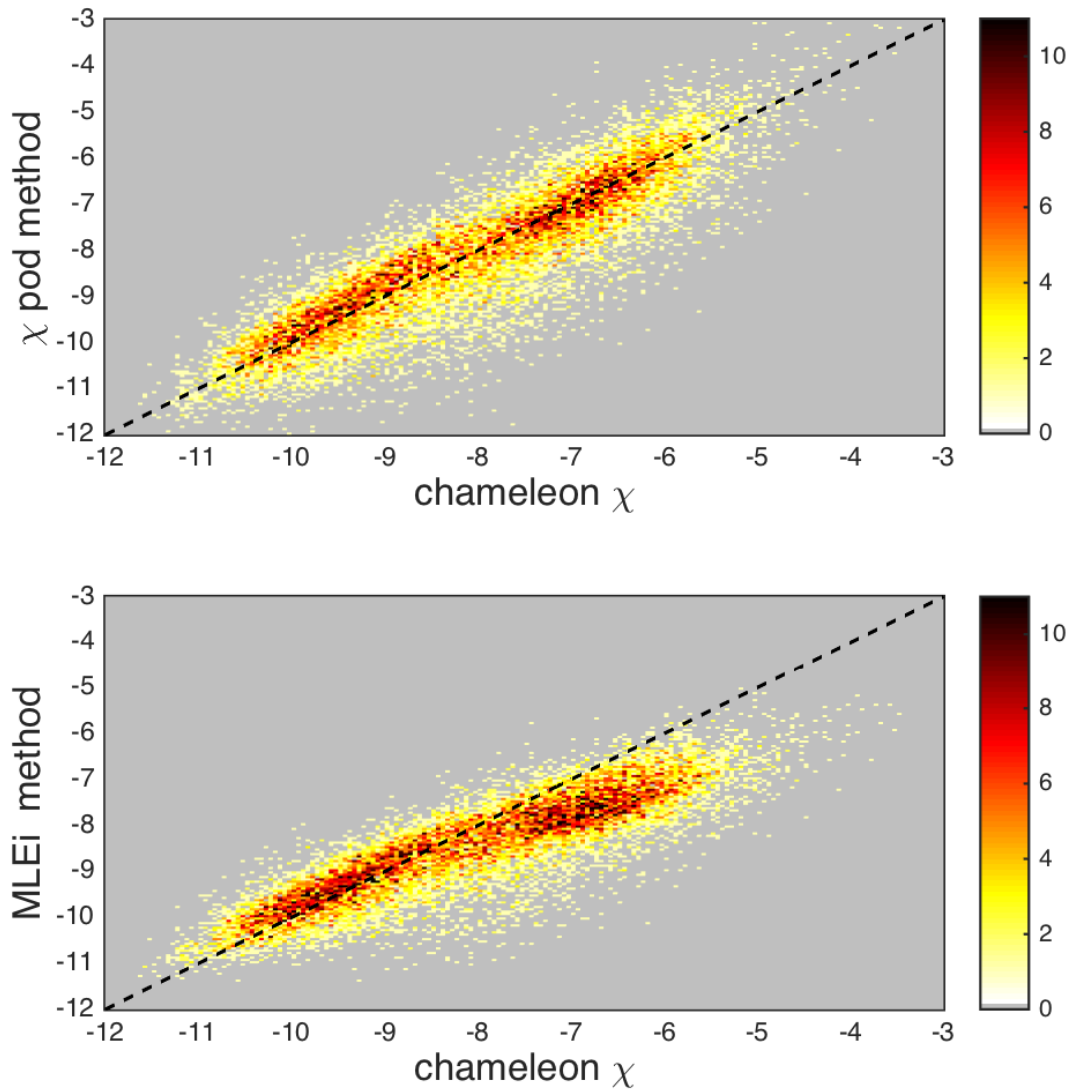


FIG. 11. Example chipod data from P16N. Top:  $dTdz$ . Bottom:  $\chi$ .



405 FIG. 12. Histogram of % error for  $\chi$  computed with constant added to fallspeed, in order to examine sensitivity  
406 to fallspeed.



<sup>407</sup> FIG. 13. 2D histograms of  $\chi$  computed using the interative  $\chi$ -pod method (top) and the MLE fit (bottom)  
<sup>408</sup> versus  $\chi$  computed from Chameleon. Note that the MLE method underestimates  $\chi$  at larger magnitudes.

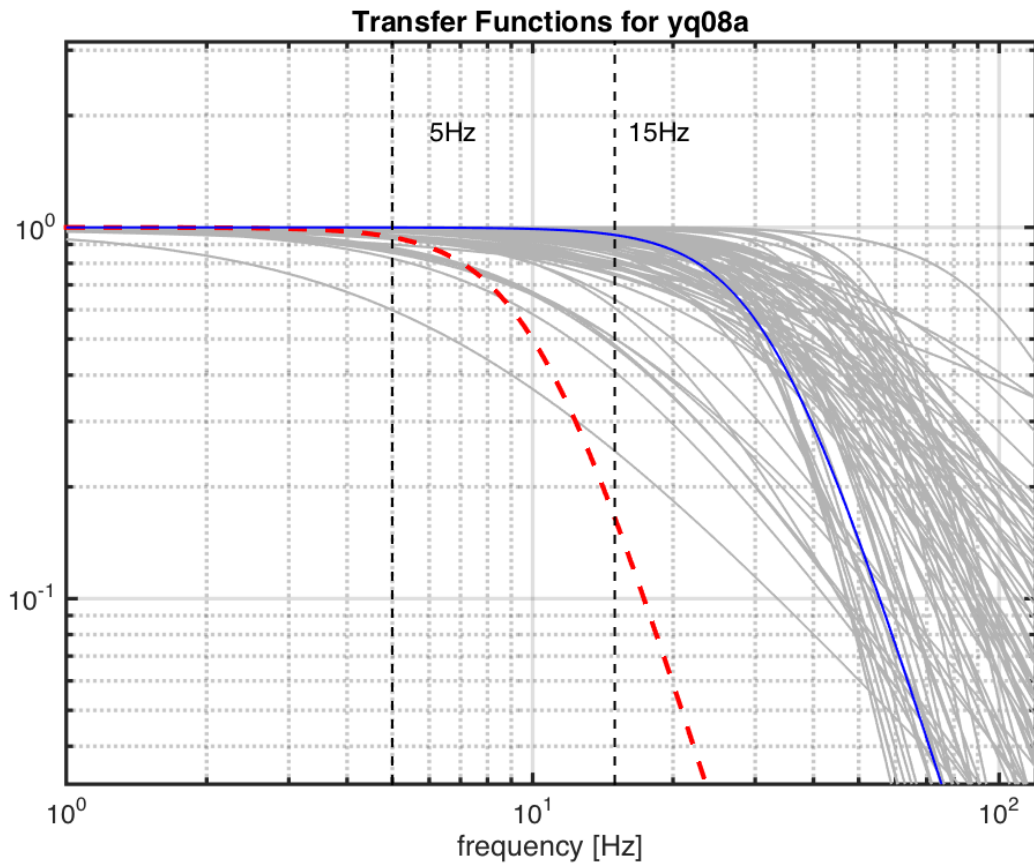
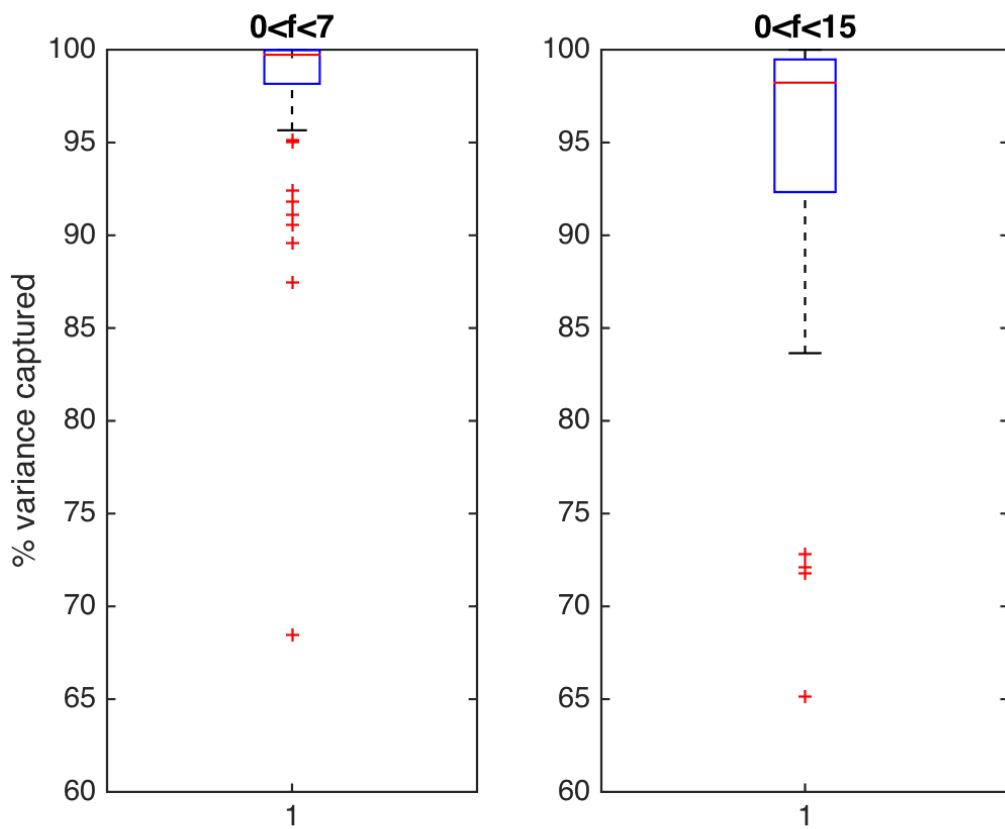


FIG. 14. Measured FP07 thermistor transfer functions.



409 FIG. 15. Boxplots of the % variance of spectra captured using no transfer function over two different ranges  
410 of frequencies. Based on transfer functions in figure 14.